Volume 1 | Number 1 | Jan 2013 | Pages 1–100

PCCP

Physical Chemistry Chemical Physics
www.rsc.org/pccp

ROYAL SOCIETY OF CHEMISTRY

ROYAL SOCIETY OF CHEMISTRY

www.rsc.org/pccp

Prospects and challenges of iron pyroelectrolysis in

magnesium aluminosilicate melts near minimum liquidus

temperature

N.M. Ferreira [1,2], A.V. Kovalevsky [1]*, S.M. Mikhalev [3], F.M. Costa [2] and J.R. Frade [1]

1 – CICECO – Aveiro Institute of Materials, Department of Materials and Ceramic Engineering, University of Aveiro, 3810-193 Aveiro, Portugal;
2 - i3N, Department of Physics, University of Aveiro, 3810-193 Aveiro, Portugal;
3 - Nanotechnology Research Division, Centre of Mechanical Technology and Automation, University of Aveiro, 3810-193 Aveiro, Portugal

* Corresponding author. Tel: +351-234370263; E-mail: **akavaleuski@ua.pt**

Abstract

Although steel production by molten oxide electrolysis offers potential economic and environmental advantages over classic extractive metallurgy, its feasibility is far from being convincingly demonstrated, mainly due to inherent experimental difficulties exerted by harsh conditions and lack of knowledge regarding relevant mechanisms and physico-chemical processes in the melts. The present work was intended to demonstrate the concept of pyroelectrolysis at very high temperature near minimum liquidus point of magnesium aluminosilicate, being conducted under electron-blocking conditions using yttria-stabilized zirconia cells, and to provide a new insight into electrochemistry behind this process. Significant current yields are possible for pyroelectrolysis performed in electron-blocking mode using solid electrolyte membrane to separate the anode and molten electrolyte. Parasitic electrochemical processes rise gradually as the concentration of iron oxide dissolved in the molten electrolytes is depleted, impairing faradaic efficiency. Reduction of silica to metallic silicon was identified as a significant contribution to those parasitic currents, among other plausible processes. Direct pyroelectrolysis without electron blocking was found much less plausible, due to major limitations on faradaic efficiency imposed by electronic leakage and insufficient ionic conductivity of the aluminosilicate melt. Ohmic losses may consume an excessive fraction of the applied voltage, thus failing to sustain the Nernst potential required for reduction to metallic iron. The results suggest the need for further optimization of the molten electrolyte composition to promote ionic conductivity and to suppress electronic transport contribution, possibly, by tuning Al/Si ratio and altering the network-forming/modifying behaviour of the iron cations.

Keywords: steelmaking, iron extraction, solid oxide membrane, electron-blocking, molten electrolyte, alloying.

Introduction

Steel is essential in huge quantities in the modern world, and its extractive metallurgy is one of the largest industrial contributors to greenhouse emissions, due to extensive use of coal as reducing agent and other fossil fuels to operate at very high temperatures. Thus, the development of alternative CO_2-lean and highly efficient technologies is critical for sustainable steelmaking.[1,2]

Although classical extractive metallurgy is well-established, and energy consumption per tonne of produced steel has been reduced by 50 % in recent years, this sector is now facing stronger pressure to lower greenhouse gas emissions, and to comply with stricter international regulations. A carbon-free alternative for steelmaking based on the use of hydrogen for reduction of iron oxide ore also raises concerns about safety and poor volume/time yield (Ref. [3] and references therein). Thus, from a broad environmental prospective, one seeks new strategies for carbon-lean iron extraction, with emphasis on electrolysis.

Pyroelectrolysis has been proposed for direct extraction of liquid iron from the oxide feedstock in molten oxides.[3-7] Operation at very high temperatures is expected to yield potential decrease in energy consumption compared to classical extractive metallurgy,[3,7] based on expectations of enhanced electrode kinetics, and mainly if one seeks nearly auto-thermal conditions. In this case, direct use of waste heat generated by electrode overpotentials and ohmic losses may account for endothermic reduction of hematite to magnetite. It has even been claimed that pyroelectrolysis opens perspectives for extraterrestrial production of oxygen, iron and silicon.[8] Although the idea itself is established, technical feasibility is far from being demonstrated, mainly due to the very corrosive nature of molten electrolytes, critical issues concerning development of suitable anode materials, and inherent difficulties in monitoring electrochemical processes at very high temperatures. Faradaic efficiency reported for iron reduction from silicate melts by direct electrolysis using $Cr_{90}Fe_{10}$ anode did not exceed 35 %,[7] showing a strong need for deeper understanding of mechanisms and further optimization of the concept to attain acceptable current yields.

Other recent approaches for less common metal electrolysis are based on solid oxide membranes (SOM) to achieve electrochemical oxygen pumping from melts.[9-13] This

process was demonstrated for electrochemical extraction of calcium and magnesium from oxide/chloride or fluoride melts at intermediate temperatures. These metals are important as reducing agents for metallothermic production of titanium and other metals from their oxides. SOM technology is based on a solid electrolyte membrane with high ionic conductivity between the anode and liquid electrolyte, allowing selective transport of the oxygen ions, and blocking the oxidation of electrochemically active species in the anode compartment.

Benefits of electrochemical pumping with SOM are expected to be reached at the highest feasible temperatures to ensure high current densities,[11] provided that this does not cause reducibility of the solid electrolyte membrane and electrochemical leakage. The most common electrolyte material is yttria-stabilized zirconia (YSZ), which possesses high ionic conductivity and appropriate stability under the harsh conditions imposed by molten electrolytes. Zirconia-based solid electrolytes also maintain reasonably wide electrolytic domains up to very high temperature. Using literature sources for temperatures in the range $1673 - 1873$ K,[14,15] one estimated values of average electronic transport below 0.01 S/cm for up to about 1827 K, under a typical oxygen partial pressure range $\sim 10^{-13} - 0.21$ atm. This corresponds to a Nernst potential of about 1.11 V, which is within the expected range required to reduce iron oxide to metallic Fe, as shown below. Actually, reduction to metallic iron was reported on the basis of oxygen permeation across the YSZ membrane,[16] i.e., with the YSZ membrane separating the anodic and cathodic compartments without direct contact with electrodes. The high applied cell voltage used in that work (4 V) was much wider than the electrochemical stability of the YSZ, causing its reducibility, onset of mixed conduction and electrochemical permeation.

In the present work, the electron-blocking ability of the solid electrolyte membrane was retained by keeping the applied voltage in the range $1.5 - 2$ V, to demonstrate the concept of Fe electrolysis under oxygen pumping conditions, using the type of cell represented in Figs. 1. This study is intended to attain better understanding of relevant mechanisms and limitations of high temperature electrochemical iron extraction. Results obtained in electron-blocking operation mode are also compared with corresponding results under direct electrolysis mode, without employing the solid electrolyte membrane.

For selection of the appropriate model-electrolyte composition, one took into account the harsh conditions of the pyroelectrolysis process, which can facilitate a large number of reactions between the electrodes and electrolyte and even interaction with YSZ membrane. Related uncertainties in the interpretation of the experimental results can be, at least, partially minimized by using a chemical composition with the minimum liquidus temperature in $MgO-Al_2O_3-SiO_2$ system,[17] thus allowing a moderate decrease in the process temperature. The selected composition corresponded to $Al_{0.374}Mg_{0.203}Si_{0.423}O_{1.61}$, which was further used as a model electrolyte system to demonstrate the pyroelectrolysis concept in the present work.

Pyroelectrolysis of iron at very high temperatures is poorly understood in what concerns electrode kinetics in molten oxides, their ionic and electronic transport properties, and dependence on composition and temperature. This includes uncertainties regarding valence states of Fe^{n+} ions dissolved in the molten oxide electrolyte, and cell voltage required for electrochemical reduction to metallic Fe without exceeding the electrochemical stability of the solid electrolyte.

One of the main issues is related to coexistence of divalent Fe^{2+} and trivalent Fe^{3+} in the molten silicate used as electrolyte,[18] and its expected impact on the ionic and electronic transport numbers. The $Fe^{2+}:Fe^{3+}$ ratio is likely to depend on glass composition,[19] with emphasis on basicity.[20]

One also expects strong correlation between redox kinetics and basicity, based on the contributions of alkaline and alkaline earth components to transport properties with obvious impact on reoxidation.[21] Humidity may also play relevant effects on the activities of divalent and trivalent Fe^{n+} species,[22] oxygen migration[23,24] and conductivity.[24]

Compilation of literature data relative to the dependence of $(Fe^{2+}:Fe^{3+})$ ratio on optical basicity of silicate melts at temperatures of about 1400 °C and in air has been described by a typical dependence:[19,26]

$$\log\left(\frac{Fe^{2+}}{Fe^{3+}}\right)^2 \approx 1.29 - 3.34x \tag{1}$$

where x accounts for summation of oxide optical basicities. For composition

$Al_{0.374}Mg_{0.203}Si_{0.423}O_{1.61}$ with 2 mol% FeO_x one expects $x \sim 0.56$ and $(Fe^{2+}:Fe^{3+}) \sim 0.52$, suggesting that trivalent Fe^{3+} may still prevail under oxidising conditions, mainly because the basicity of the actual composition is low. Other relevant information can be extracted from literature data for the solubility of divalent $X_{FeO_{(s.m.)}}$ and trivalent oxides $X_{FeO_{1.5-\delta((s.m.)}}$ in natural silicate melts ([27-29] and quoted references). Indeed, redox changes may occur on cooling, and one found evidence that divalent Fe^{2+} may still prevail in the actual composition, at least for samples cooled in air at high pulling rates.[30] Still, one considered the dependence on temperature (T), oxygen fugacity (f_{O2}) and contents of basic components (X_i) proposed elsewhere:[27]

$$\ln\left(\frac{X_{FeO_{1.5-\delta((s.m.)}}}{X_{FeO_{(s.m.)}}}\right) \approx 0.232\ln(f_{O_2}) + \frac{48.3x10^3}{T} - 23.2 - \frac{\sum_i X_i \Delta\mu_i}{RT} \tag{2}$$

with chemical potential contributions $\Delta\mu_i$=49.04 kJ for Al_2O_3, - 48.87 kJ for CaO, - 106.05 kJ for Na_2O.

The dependence on redox conditions in Eq. 2 is close to the expected dependence for nearly ideal or regular behaviour in dilute conditions:

$$FeO_{(s.m.)} + 0.25O_2 \Leftrightarrow FeO_{1.5(s.m.)} \tag{3}$$

Thus, one also expects depletion of oxygen fugacity for representative conditions of SOM operation, i.e., when the inner electrode (1) in the YSZ-based cell (Fig. 1) is polarized cathodically, and the outer electrode (3) is polarized anodically. The highest oxygen fugacity in the silicate melt is expected at the melt/YSZ interfaces and, on assuming that the YSZ membrane is a pure oxygen ion conductor, with the external electrode in air, this may be given by the Nernst equation:

$$P_{O_2,i} \approx 0.21\exp\left\{-\frac{4F(\eta_i + R_{YSZ}I + \eta_3)}{RT}\right\}atm \tag{4}$$

Note that total losses relative to the external reference (0.21 atm) combine ohmic losses in the YSZ electrolyte ($R_{YSZ}I$), overpotential of the outer electrode (η_3) and, probably, also interfacial losses at the melt/YSZ interface (η_i).

The activity of divalent iron in the silicate melt $a_{FeO}^{sil.m.}$ and its dependence on basicity may

also affect redox conditions required for the onset of metallic Fe, at the inner cathode. Equilibrium conditions for co-existence of metallic Fe with the melt can be described by:

$$2Fe + O_2 \Leftrightarrow 2FeO_{sil.melt} \tag{5}$$

and

$$f_{O_2,c} = \left(X_{FeO}\gamma_{FeO}^{sil.m.}\right)^2 \exp\left(\frac{\Delta G^o}{RT}\right) \tag{6}$$

where $\Delta G^o = -488.24 - (0.01695 \times \ln(T) - 0.2311)$, is the free energy of reaction: $2Fe + O_2 \Leftrightarrow 2FeO_{liq}$, and the activity coefficient of FeO in the silicate melt may be described by the empirical dependence:[31]

$$\gamma_{FeO}^{sil.m.} = \sum_{j=1}^{4}\sum_{k=1}^{j} a_{jk}X_j X_k \tag{7}$$

For the actual composition $Al_{0.374}Mg_{0.203}Si_{0.423}O_{1.61}$ with 2 mol% FeO one obtain $\gamma_{FeO}^{sil.m.} = 1.20$ at ~ 1400 ºC, and on inserting this in Eq. 6 one predicts $f_{O_2} \approx 10^{-13}\, atm$. This also yields the corresponding Nernst potential relative to air (1.02 V). Further additions of iron oxide yield $fO_2 \sim 3.8 \times 10^{-13}$ atm for 4 mol% FeO, $fO_2 \sim 1.42 \times 10^{-12}$ atm for 8 mol% FeO, etc.
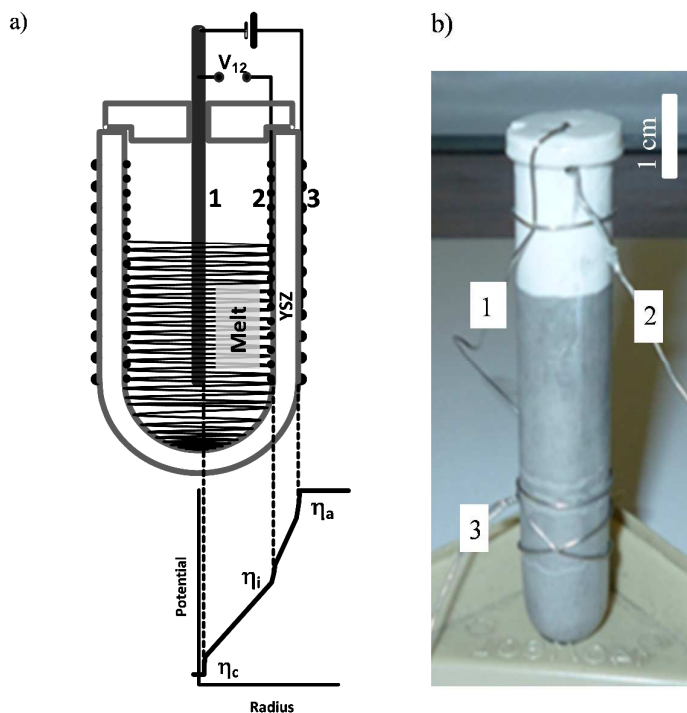
Figure 1 – a) Schematic representation and b) phototograph of the electron-blocking cell used for iron pyroelectrolysis.

The contents of iron oxide and (Fe^{2+}:Fe^{3+}) ratio may determine the ionic and electronic transport properties. However, the relative contributions also depend on mobility of these cationic species in silicate glasses, which depends on their prevailing structural incorporation as network formers or modifiers. Glass former cations form structural tetrahedral units ($[SiO_4]^{4-}$, $[AlO_4]^{5-}$,…..) with very low mobility. This also applies partially to Fe^{3+}, with mixed character between network former $[FeO_4]^{5-}$ and modifier.[32,33] Thus, Fe^{2+} should have a prevailing contribution to ionic conductivity, due to its network modifier character, probably combined with the additional contribution of Mg^{2+}, at least if one considers ac electrical response. Otherwise, dc electrical behavior should be mainly dependence on migration of Fe^{2+} if the applied voltage exceeds the Nernst potential for reduction to metallic Fe, possibly combined with an additional electronic contribution by small polaron hopping between ferric and ferrous ions.[34] Redox stable mobile cations (e.g. Mg^{2+}) are likely to give rise to space charge effects. These factors were mostly taken into account, when analysing the results, obtained in the present work.

Experimental

Powders of MgO (Merck, 99+ %), Al_2O_3 (Merck, 99.5 %), SiO_2 (Sigma Aldrich, 99.6 %) were mixed in required proportion to obtain the nominal composition $Mg_{0.203}Al_{0.374}Si_{0.423}O_{1.61}$ (MAS – Magnesium Aluminosilicate) with minimum liquidus temperature. The required amounts of Fe_3O_4 (Aldrich, 99 %) was added to prepare the corresponding composition with 2 mol% of Fe. After addition of a binder (PVA) the prepared mixtures were extruded as feed and seed precursor rods to prepare the intended glasses by laser floating zone (LFZ) method. Amorphous samples were grown at 100 mm/h using a continuous CO_2 Spectron SLC laser (λ = 10.6 μm; 200 W). During the process the seed and feed rod precursors were rotated in opposite directions to enhance the homogeneity of the target samples. Obtained samples were then crashed and ball-milled in ethanol to produce a fine glass powder, which was further used as the molten electrolyte in pyroelectrolysis. Preliminary experiments showed that the obtained glass composition can be melted at temperatures above 1700 K.

Pyroelectrolysis was studied using an electrochemical cell made of yttria-stabilized zirconia (YSZ) shown schematically in Fig. 1. The cell comprised an YSZ closed-end tube and three Pt electrodes (1 to 3) to perform electrolysis studies in various regimes and to evaluate the resistance of molten electrolyte by impedance spectroscopy. The cells were loaded with 3.6 to 4.8 g of the glass electrolyte powder, prepared as described above. After filling the internal compartment with electrolyte and centering the electrode (1) wire ($\varnothing$ 0.5 mm), the cell was closed by an YSZ lid and vertically aligned in an external alumina crucible and held vertically with alumina powder. The distance between electrode (1) and bottom of the cell was circa 5 to 7 mm. Thus assembled cell was heated up to 1728 K at a rate of 5 K/min. Onset of melting was monitored by rapid drop in resistance between electrodes 1 and 2, measured under open-circuit condition by electrochemical impedance spectroscopy (Autolab PGSTAT302 instrument, frequency range 0.01 to 10^6 Hz). Fig. 2 shows corresponding Nyquist plots during electrolysis process. Above 1700 K the shape of the impedance spectra significantly changes, while the resistance of the cell dramatically decreases.
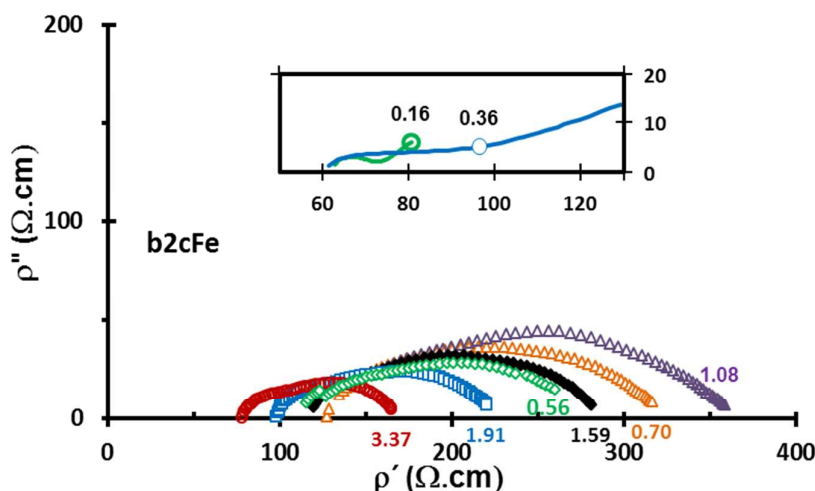
Figure 2 – Complex resistivity spectra (see Eq.12) for b2cFe cell, obtained after different relative charging, i.e., Q/Q_{Fe} = 0.16 (inset), 0.36 (inset), 0.56, 0.70, 1.59, 1.91 and 3.37, where Q_{Fe} denotes the charge required to reduce the actual content of iron oxide to metallic Fe, assuming that Fe^{2+} prevails, based in eqs 1.12 and 1.13.

Table 1 shows the relevant experimental conditions of the pyroelectrolysis experiments. These studies were preceded by preliminary experiments, which were required to screen appropriate procedures for the preparation of cells, conditions for high-temperature electrochemical measurements, risks of short-circuiting in the cell, caused by displacement of the central electrode wire (1), etc. In electron-blocking cell experiments, a constant dc voltage was applied between the Pt wire cathode (1) and the external counter electrode (3). Other experiments were performed in direct electrolysis mode between cathode (2) and anode (1), i.e., without electron blocking. The changes in electrochemical properties of the cell components were also monitored by impedance spectroscopy, between electrodes (1) and (2). These spectra (see Fig. 2) were acquired without dc bias, by temporarily disconnecting the applied dc voltage, for 2 to 3 min, to ensure sufficient signal to noise ratio. The results were further assessed in terms of the time dependencies of the electrolysis current and accumulated electrical charge, aiming on rough estimation of the Faradaic efficiency by analysis of the transient electrochemical response of the cell. Periodical switching of the applied dc voltage resulted in appearance of current spikes on the corresponding current-time curves, which are further discussed below.

After the pyroelectrolysis experiments the cells were cooled down to room temperature at 5 K/min, for subsequent post-mortem analysis. The bottom part of the cell, containing

solidified electrolyte, was cut transversely by a diamond wafering blade into 3 to 5 pieces, to analyse the cation distribution in the cathodic compartment and to assess the approximate liquid electrolyte level during the pyroelectrolysis process. The cut pieces were polished and examined by combined SEM/EDS studies (Hitachi SU-70 model equipped with Brucker silicon drift EDS detector).

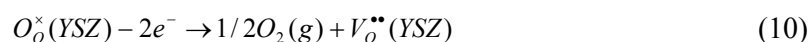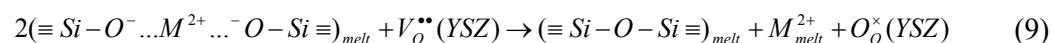**Table 1 – Operating regimes and other relevant experimental conditions for the electrochemical cells.**

Notation	Regime	Cathode	Anode	V_{appl} (V)	FeO_x additions
b2cFe	Electron-blocking	(1)	(3)	2.0	2 mol%
b1.5cFe	Electron-blocking	(1)	(3)	1.5	2 mol%
b1.5c	Electron-blocking	(1)	(3)	1.5	Fe-free
d1.5aFe	Direct-electrolysis	(2)	(1)	-1.5	2 mol%

The element distribution in the polished samples were examined also by Raman spectroscopy (Horiba Jobin Yvon 800HR) at room temperature in backscattering configuration, using the 532 nm exciting line, from 100 to 1000 cm^{-1}, and a lens magnification of x100 with an aperture of 0.9 and a spot size of 1 μm.

Results and Discussion

Proposed equivalent circuit

Under electron-blocking operation mode, the YSZ membrane separates the cathodic and anodic compartments, and is expected to block the electronic transport. This allows selective transport of oxygen ions and should prevent iron reoxidation at the anode. Iron cations migrate in the molten silicate under the applied electric field and are expected to be reduced to metallic Fe at the cathode, when the applied voltage exceeds the minimum Nernst cell voltage, while the oxygen ions are likely to be transferred across the molten silicate/YSZ interface, migrate through the YSZ solid electrolyte by a vacancy mechanism, and feed the oxygen evolution reaction at the outer electrode. Thus, the actual concept of pyroelectrolysis with electron blocking provided by YSZ can be approximately described on assuming the following half-cell cathodic (electrode 1) and anodic (electrode 3) reactions, coupled with partial conversion of non-bridging to bridging oxygen ions in the molten silicate and ion transfer across the silicate melt/YSZ interface:

$$Fe^{2+} + 2e^- \rightarrow Fe^0 (Pt) \tag{8}$$

$$2(\equiv Si - O^- ... M^{2+} ...^- O - Si \equiv)_{melt} + V_O^{\bullet\bullet}(YSZ) \rightarrow (\equiv Si - O - Si \equiv)_{melt} + M_{melt}^{2+} + O_O^\times(YSZ) \tag{9}$$

$$O_O^\times(YSZ) - 2e^- \rightarrow 1/2O_2(g) + V_O^{\bullet\bullet}(YSZ) \tag{10}$$

Note that divalent Fe^{2+} is expected to prevail in the molten silicate glass electrolyte under conditions of electrochemical oxygen pumping, which depresses O_2 fugacity, at least near the Pt cathode. Thus, one can assume that pyroelectrolysis with electronic blocking involves partial transfer of non-bridging oxygen ions from the melt to the solid electrolyte, according to reaction of Eq. 9, with simultaneous migration of the modifier cations in opposite direction, towards the inner cathode.

A schematic representation of a possible equivalent circuit for the overall behaviour is presented in Fig. 3. Equivalent circuits have been proposed to analyse mixed conduction in solids.[35] Though this is arguable in the present case, due to scarce information and excessive experimental scattering, one may still assume association of a prevailing contribution of ionic transport and a parallel contribution of electronic transport, with

series associations of components in the molten electrolyte and in the YSZ solid electrolyte, i.e., $R_{I,m}+ R_{I,s}$, respectively.
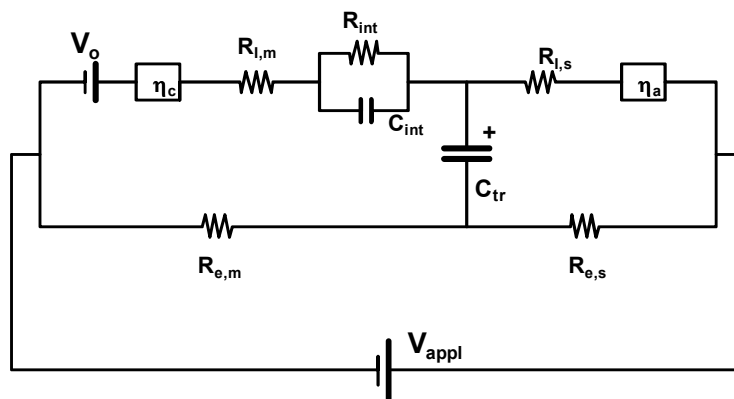

Figure 3 – Proposed equivalent circuits for electron-blocking cell.

The equivalent circuit in Fig. 3 also includes expected cathode (η_c) and anode (η_a) overpotential contributions, and an interfacial contribution, based on the intermediate frequency arc revealed by impedance spectra (Fig. 2). This may be nearly accounted for by the $R_{int}C_{int}$ component in the equivalent circuit, or a corresponding constant phase element (CPE) taking into account that interfacial arcs are usually depressed (e.g. Fig. 2). In addition, the YSZ solid electrolyte allows selective oxygen ion transport and should be nearly blocking to the electronic conductivity and to contributions of redox stable cations (e.g. Mg^{2+}), this was accounted for by inserting a capacitor in the equivalent circuit (C_{tr}).

The cell voltage must exceed a lower limit corresponding to the Nernst potential generated by oxygen fugacity ratio between the surrounding atmosphere (0.21 atm), and the silicate melt in the presence of metallic Fe. For a typical temperature of about 1728 K and based on Eq. 6, with a typical activity coefficient $\gamma_{FeO}^{sil.m.} =1.20$ (for 2 mol% iron oxide), one estimated $fO_2 \sim 2.7 \times 10^{-13}$ atm, and the corresponding value of Nernst potential:

$$E_o = \frac{RT}{4F}\ln\left(\frac{0.21}{2.7x10^{-13}}\right) \approx 1.02\,V \tag{11}$$

Ohmic losses are likely to be one of the main limitations in energy efficiency due to insufficient ionic conductivity. One expects major dependence on the inner electrode under the actual nearly cylindrical geometry, due to major differences between the inner

(r_i) and outer electrode (r_e) radii, with corresponding impact on electric field, current density differences, and gradient of ohmic losses. This gradient is much steeper near the central electrode, as derived on assuming a steady state regime with nearly cylindrical geometry and without radial changes in conductivity, i.e., $\sigma(dV/dr) \approx I/(2\pi rL)$, where I is current, L is length and r is radial distance. On integrating, one obtains the relevant solutions for ohmic resistance and electric field:

$$R = \frac{\Delta V_{ohmic}}{I} \approx \left[2\pi L\sigma \ln\left(\frac{r_e}{r_i}\right) \right]^{-1} \tag{12}$$

and

$$\frac{dV}{dr} \approx \frac{\Delta V_{ohmic}}{r \ln(r_e/r_i)} \tag{13}$$

where ΔV_{ohmic} is the overall ohmic drop. Thus, the actual geometry is suitable to identify differences between specific electrode limitations under cathodic and anodic polarization, even for conditions when the use of a reference electrode is impaired by very harsh operating conditions.

Faradaic efficiency may also be affected by an onset of electronic conductivity, as shown in the proposed equivalent circuit in Fig. 3, except possibly for conditions when the electronic conductivity of YSZ is negligible and provides almost perfect blocking for electronic leakage.

This condition may be assessed by combining the dependence of n-type and p-type contributions in YSZ,[36] including high temperature results:[14]

$$\sigma_n = 1.65 \times 10^6 \exp\left(-\frac{3.85\text{eV}}{kT}\right)(pO_2)^{-1/4} = \sigma_{n,o}\,(pO_2)^{-1/4}\,\text{S/cm} \tag{14}$$

$$\sigma_p = 27 \exp\left(-\frac{1.40\text{eV}}{kT}\right)(pO_2)^{1/4} = \sigma_{p,o}\,(pO_2)^{1/4}\,\text{S/cm} \tag{15}$$

The corresponding average value can be computed for the relevant boundary conditions pO_2' and pO_2'':

$$\sigma_{e,av} = \frac{4}{\ln\left(\frac{pO_2''}{pO_2'}\right)} \int_{pO_2'}^{pO_2''} \left(\sigma_n + \sigma_p\right) d\ln(pO_2) =$$

$$= \frac{4}{\ln\left(\frac{pO_2''}{pO_2'}\right)} \left\{\sigma_{n,o}\left[\left(pO_2'\right)^{-1/4} - \left(pO_2''\right)^{-1/4}\right] + \sigma_{p,o}\left[\left(pO_2''\right)^{1/4} - \left(pO_2'\right)^{1/4}\right]\right\} \qquad (16)$$

yielding a typical value for electronic conductivity of YSZ ($\sigma_{e,av} \sim 2.8 \times 10^{-3}$ S/cm) under the actual working conditions, i.e., at 1728 K, and on assuming limiting conditions for air ($pO_2 = 0.21$ atm), and equilibrium between metallic Fe and molten electrolyte ($\sim 2.7 \times 10^{-13}$ atm).

The ionic resistance in the YSZ solid electrolyte may also be estimated by considering literature data for ionic conductivity of YSZ at very high temperatures.[15]

$$\sigma_I = 1.95 \times 10^5 \, T^{-1} \exp\left(-\frac{0.74\text{eV}}{kT}\right) \text{S/cm} \qquad (17)$$

with a typical value of 0.79 S/cm at 1728 K. This is more than 2 order of magnitude higher than the electronic conductivity, which confirms that YSZ should provide electronic blocking.

In addition, the ionic conductivity of YSZ is close to 2 orders of magnitude higher than the actual order of magnitude of conductivity of the molten electrolyte, extracted from the impedance spectra (e.g., Fig. 2). These impedance spectra are shown as complex resistivity plots for cylindrical symmetry (Eq. 12), i.e.:

$$\rho_{I,m} \approx \frac{2\pi L R_{I,m}}{\ln\left(d_i/d_o\right)} \qquad (18)$$

where d_i is the inner diameter and d_o the outer diameter of the YSZ cell.

Results in Fig. 2 are in the order of 10^2 Ωcm, which is a significant limitation for pyroelectrolysis with the actual molten electrolyte. Note that basaltic melts attain similar conductivity values at significantly lower temperatures ($\sim$ 1573 K).[37] This can be understood by taking into account that the mobility of prevailing carriers in the actual aluminosilicate melts (Fe^{2+} and Mg^{2+}) may be much smaller than the mobility of alkali carriers in basaltic melts, as revealed by corresponding diffusivity ranges.[21] The structure of molten silicates can be described as three-dimensional interconnected network of

$[SiO_4]^{4-}$ tetrahedra, where the silicon atoms are mostly joined by bridging oxygen atoms $(\equiv Si-O-Si\equiv)_{melt}$,[38] whereas alkaline ($Na^+$, ...), alkaline earth ($Mg^{2+}$,...) and other cations (Fe^{2+},...) provide charge compensation for non-bridging oxygens and may act as ionic charge carriers.

Post-mortem analyses

Although one attempted to estimate Faradaic efficiency by direct weighing the cathode after iron extraction and quantifying the volume of gaseous species, evolved at the anode, such measurements have particular difficulties under the extremely harsh experimental conditions of pyroelectrolysis, with emphasis on disintegration of the Pt cathode and changes in morphology (Fig. 4). In addition, estimates of Faradaic efficiency are affected by uncertainties concerning the initial distribution of Fe^{2+} and Fe^{3+} in the aluminosilicate melt and their changes on lowering the oxygen fugacity by electrochemical pumping. Therefore, in the present work one relied mostly on post-mortem analysis of the cell by combining SEM (Fig. 4) and EDS analyses (Fig. 5), and results of electrochemical measurements, to confirm electroreduction to metallic Fe.

Somewhat surprisingly, Fig. 4 shows drastic degradation of the Pt cathode, in contrast with the reference Pt electrode. The Pt cathode disintegrated in isolated segment in the cross section, including small spots organized in ring-like distribution. Smaller dispersed fragments are also found in the surrounding area, as shown in the expanded SEM image.

Still, the total cross section of the remaining Pt fragments is significantly smaller than the initial cross section of the Pt wire.

The circular area traced by Pt fragments is also surrounded by the Al-rich and Si-deficient ring. In addition, high Fe-concentrations are found both inside this ring, mostly overlapping with the Pt elemental map, and in the surrounding area. One may speculate that dispersed Fe-rich fragments correspond to metallic Fe, based on their spatial distribution.
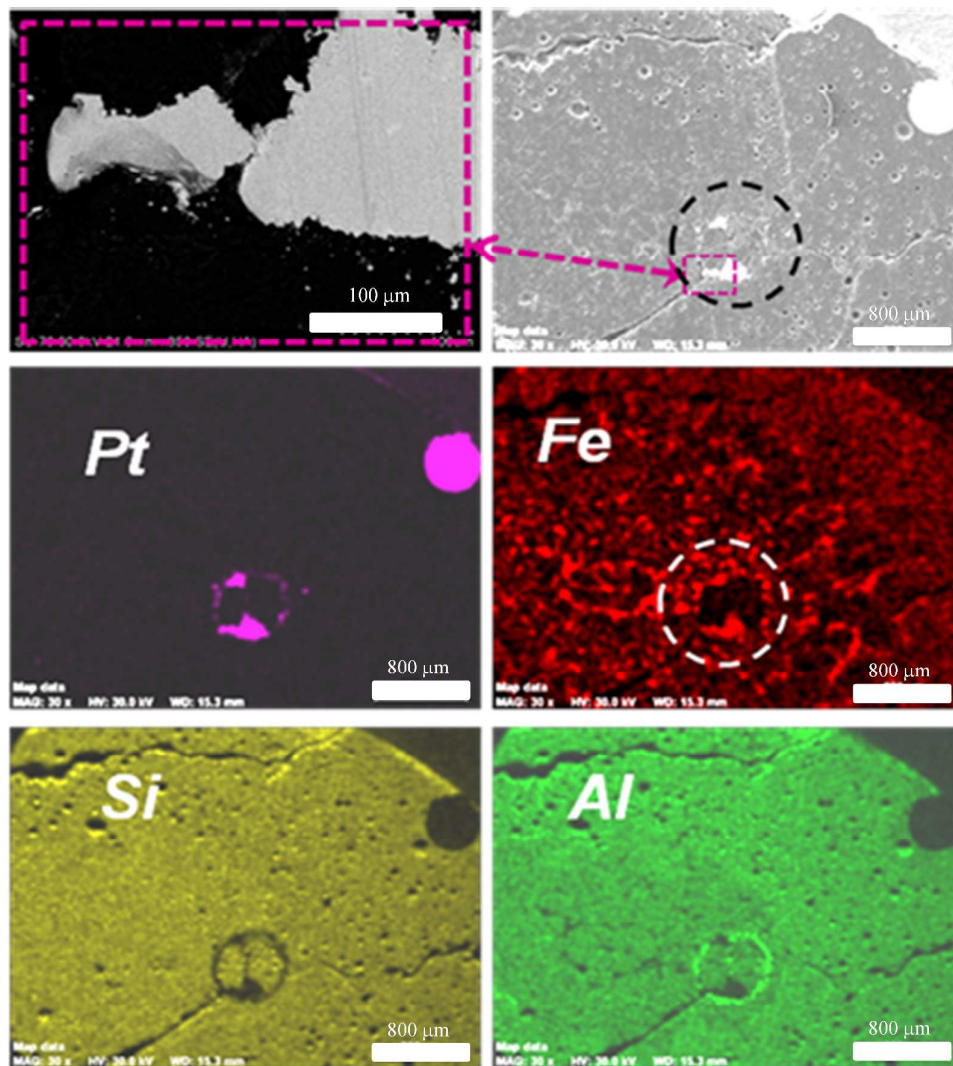
Figure 4 – Post-mortem SEM microstructures and elemental maps of the pyroelectrolysis cell b2cFe, tested with applied cell voltage of 2.0 V.
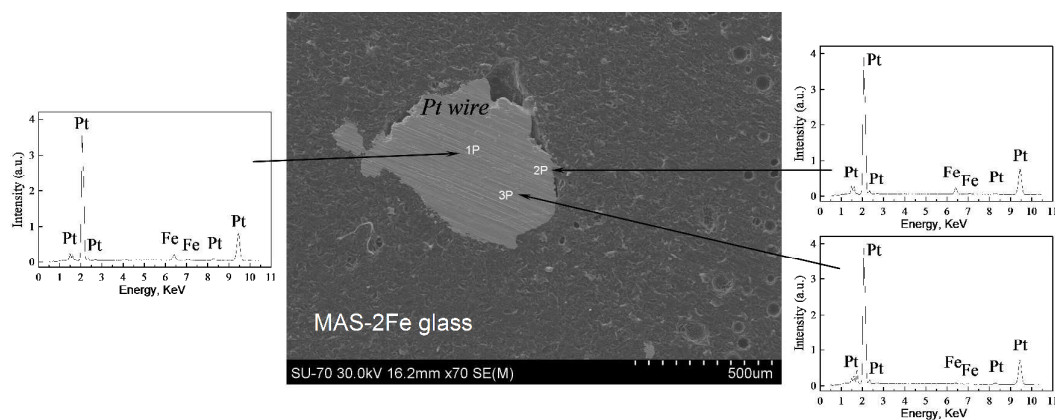

Figure 5 – Post-mortem EDS analysis of b2cFe cell.

17

Note that the expected cross section of metallic Fe deposit should be in the order of 0.3 mm^2, if one considers complete reduction of the iron oxide content in the melt. Though one could not confirm the nature of these Fe-rich spots the surrounding area, they resemble onset of metallic Fe inclusions reported for aluminosilicate melts exposed to reducing atmospheres.[39,40] Dispersed metallic inclusions are also found in basaltic rocks.[41]

Less drastic degradation of the Pt cathode, and clearer evidence of Pt-Fe alloying is demonstrated by post-mortem analysis of cell b1.5cFe, after pyroelectrolysis with applied voltage 1.5 V (Fig. 6). The Al-rich boundary is also shown in this case, and EDS spectra (Fig. 6) confirm alloying of Pt with Fe. Alloying of Pt with Fe extended to the bulk of the original Pt wire, with atomic Pt : Fe ratio of about 6.3:1, preserving the metallic appearance (color, luster, etc.), as expected for metallic alloys. Formation of Pt-Fe alloys was also reported for electrodeposition of Fe^{2+} on Pt electrodes in chloride melts at 973 – 1023 K.[18] In addition Pt-Fe alloys have been proposed as containers for silicate melts, to avoid losses of iron.[42,43]

Indeed, alloying with Fe and disintegration of Pt electrodes requires cathodic polarization, sufficient to induce reduction to metallic Fe, being hindered without application of electric field (Fig. S1, ESI), and also under anodic polarization. Thus, the physical or electrochemical nature of actual disintegration of Pt electrodes cannot be ascribed to oxidation of Pt, and is more consistent with incorporation of Pt on metallic inclusions in silicate melts under reducing conditions .[41] Post-mortem analyses are also more consistent with formation of low melting liquid phase in the ternary system Pt-Fe-Si. Note also that the actual temperature (1728 K) is lower than required for liquid phase formation in the binary Pt-Fe system.

Though reduction of silica to metallic Si and diffusion into the metallic phase might seem somewhat surprising, under a relatively low applied cell voltage (1.5 V), one finds evidence in the literature for alloying of metallic Fe with Si on exposing aluminosilicate melts to reducing atmospheres such as $CO-CO_2$[40] or H_2-Ar.[44]

Partitioning of Si between the Fe-based earth´s core and silicate melts on earth´s mantle is also known.[45] In addition, SiO_2 can be reduced to metallic silicon by pyroelectrolysis in chloride halide melts.[46] However, the solubility of Si in solid Pt is only about 1

atm%[47] thus explaining why the EDS signal of Si remains very weak in Pt-rich spots. On the contrary, one may expect a wide range of compositions for liquid phase formation in the Pt-Si system at the actual temperatures (~ 14 – 100% mol. Si).[47] At the same time, the EDS results clearly confirm absence of alloying between Pt and Fe without applied polarization (Fig. S1, ESI).
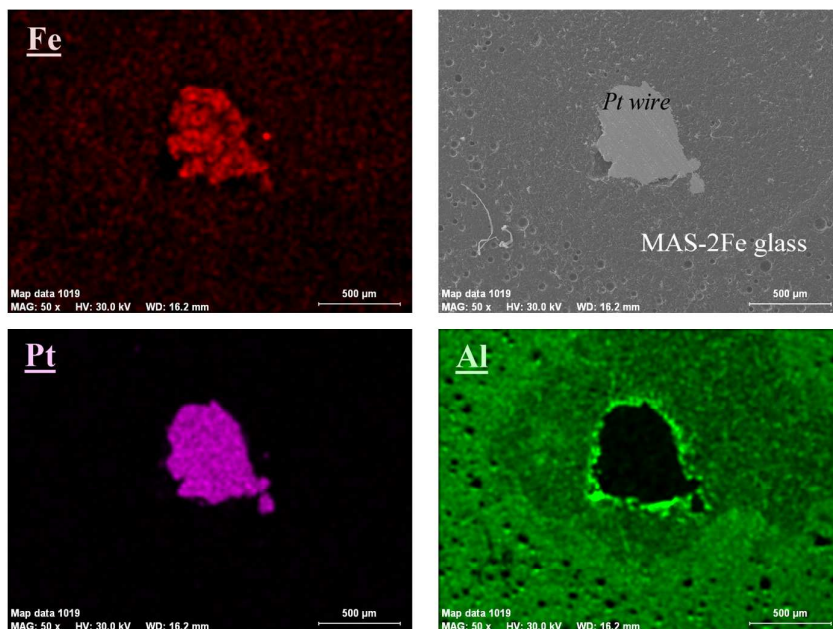

Figure 6 – SEM and elemental maps obtained by post-mortem analysis of a Pt cathode after testing b1.5cFe cell with applied cell voltage 1.5 V.

Thus, onset of a liquid phase is expected on increasing the contents of reduced Si, and this may explain disintegration of the Pt cathode and its dispersion as small droplets in the surrounding aluminosilicate melt. This may also explain onset of dispersed metallic particles shown in Fig. 4, at sufficiently high magnification. The relevant literature also showed evidence for the dynamic behaviour of Pt-Si liquid phases.[48,49]

Simultaneous reduction of Si and Fe may also explain the Al-rich ring in Figs. 4 and 6, possibly yielding liquid phase at the actual high temperatures, as predicted by the binary Fe-Si phase diagram,[50,51] and also contributing to dispersion of metallic inclusions in the area surrounding the Pt cathode. Thus, disintegration of the Pt cathode may be ascribed to liquid phase formation in the ternary system Fe-Si-Pt, and its dispersion in the surrounding area, mainly for cell b2cFe, when the applied voltage is highest and most likely to reach conditions for reduction to metallic Si. The enhanced wetting of metallic

surfaces (Fe, Pt,...) by aluminosilicate melts[44] may also contribute to ready dispersion of liquid metallic drops.

Thermodynamic and electrochemical conditions for reduction of silicon dioxide to metallic silicon or silicon monoxide can also be estimated based on relevant thermodynamic data.[52] This has been summarized in Table S1 (ESI), which shows the Gibbs free energy ΔG_R of plausible reactions at 1728 K, and corresponding Nernst $\Delta G_R/(nF)$ potential relative to standard conditions, i.e, for $pO_2 \sim 1$ atm and considering unit activity ratio $a_{SiO2} : a_{Si}$ for silicon dioxide and silicon. Thus, reduction of silica to SiO or Si is likely to occur when the pyroelectrolysis cell is operated at $V_{appl} = 2$ V. Indeed, this is unlikely for redox stable trivalent aluminium Al^{3+}, with prevailing glass former character, and also for redox stable Mg^{2+}, with prevailing modifier-character. The mobility of modifier cations may contribute to minimize the concentration gradient of magnesium. Reduction of silicon dioxide to metallic Si may still occur on lowering the applied voltage to $V_{appl} = 1.5$ V, mainly if one considers a relatively low activity ratio $a_{Si}/a_{SiO2} \ll 1$, a_{Si} being the activity of Si in the metallic liquid phase, and a_{SiO2}, the activity of silica in the MAS melt, i.e.:

$$(SiO_2)_{MAS} \rightarrow (Si)_{lm} + (O_2)_{MAS} \tag{19}$$

$$V'_o = V_o + \frac{RT}{4F} \ln \left\{ \left(\frac{a_{Si,lm}}{a_{SiO2,MAS}} \right) pO_2 \right\} < V_o \tag{20}$$

EDS spectra in Fig. 6 even suggest the presence of Al in the postmortem analysis of the Pt-cathode, possibly as an artifact resulting from polishing. In fact, the redox stability of alumina should prevent reduction to metallic Al, except possibly for relatively high applied cell voltage, as emphasized by the Gibbs free energy of the relevant reaction and corresponding Nernst potential (Table S1, ESI). Still, one cannot rule out the possibility of reduction of alumina for cell b2cFe, operated under applied of 2V. Note that the presence of Al in ternary Fe-Si-Fe would also contribute to suppress the liquidus temperatures of metallic inclusions.[51] Prospects for reduction of aluminium oxide to metallic Al were demonstrated for redox conditions corresponding to very dry hydrogen ($H_2 : H_2O > 10^5$), possibly assisted by volatile intermediate species (AlH or Al_2O).[53]

Evidence that disintegration of the Pt cathode may be induced by reduction to elemental

Si and formation of Si-Pt liquid phase may also be inferred from micro-Raman spectra (Fig. 7a). Spectra localised on residual fragments of the Pt cathode, as represented by an illustrative SEM image (Fig. 7b), show a main peak at ~ 480 cm^{-1}, which is close to the characteristic transverse optical band of amorphous silicon,[54] and is absent in the Raman spectrum of the MAS matrix. Though one cannot exclude the presence of this peak in the Raman spectrum obtained for original Pt wire, this is close to the background noise.

Thus, this does not contradict the evidence that disintegration of the Pt cathode may be induced by alloying and formation of liquid phases, probably in the ternary Pt-Fe-Si system. Note also that the active Raman bands of the MAS matrix (~ 253 cm^{-1}, 567 cm^{-1} and 673 cm^{-1}) vanish in the proximity of the remaining spots of the Pt cathode.
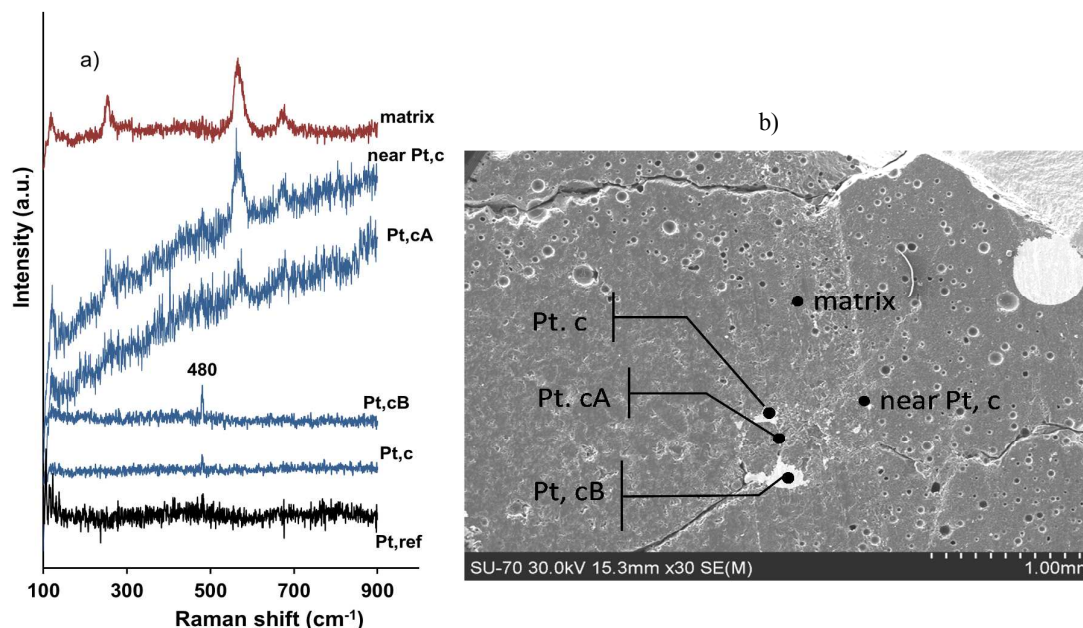

Figure 7 – a) Raman spectra and b) SEM microstructure of b2cFe cell, located at the MAS matrix, reference Pt wire (Pt,ref), major spot of the Pt cathode (Pt,c), smaller Pt spots (Pt,cA and Pt,cB), and a nearby location (near PT,c). Notice, that provided SEM image is only an illustration to show the relative positions of the analyzed points.

Cell (b1.5c) was operated in blocking-electron configuration with Fe-free MAS glass electrolyte, while keeping the remaining conditions similar to cell b1.5cFe (Table 1). In

this case, the Pt cathode remains relatively immune to disintegration, as shown in Fig. 8.
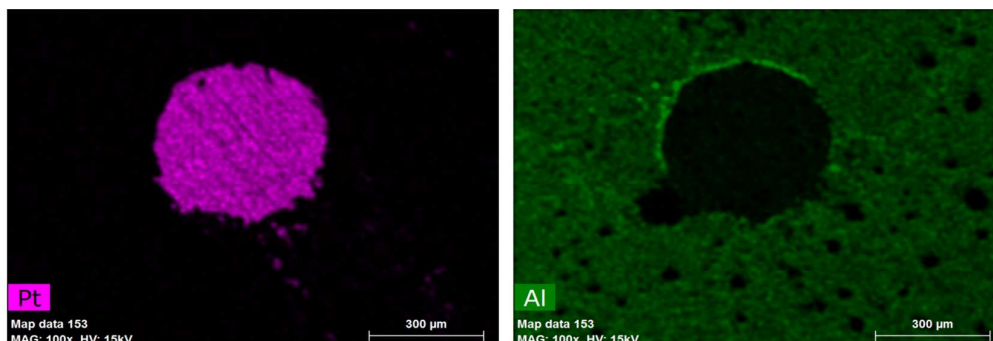

Figure 8 – Pt and Al elemental maps of b1.5c cell.

Note that traces of Pt towards the bottom-right of this map are an artefact due to cutting of the sample. Thus, the presence of Fe in Pt-based alloys play a key role in the disintegration of the Pt cathode observed for the previous cells (b2cFe and b1.5cFe). In addition, enhanced wetting of cathode by the aluminosilicate melt is expected upon incorporation of Fe in the metallic phase,[44] possibly contributing to assist incorporation of Si and formation of liquid phase in the ternary system Pt-Fe-Si, responsible for the disintegration of the cathode in cells b2cFe and b1.5cFe.

Additional evidence that disintegration of the Pt electrode is specific for cathodic polarization was provided by reversing the polarization of the central Pt electrode to anodic in the cell d1.5aFe (Table 1). In this case, anodic polarization also prevents disintegration, as shown in Fig. 9.
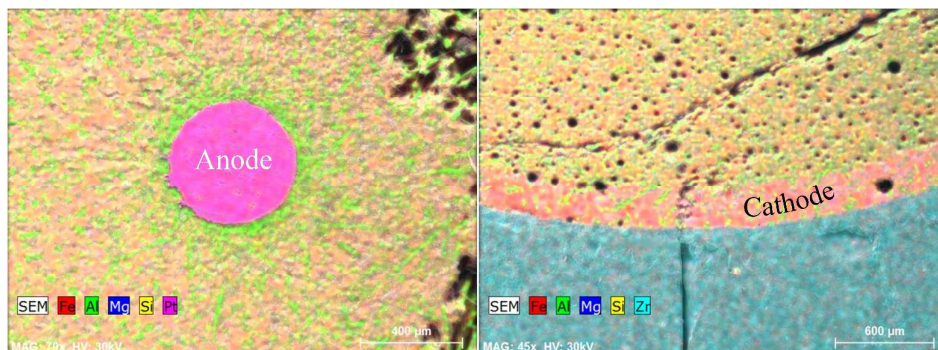

Figure 9 – Post-mortem elemental maps of d1.5aFe cell.

Note also that the surrounding aluminosilicate melt still becomes Al-rich, probably by

migration of Fe^{2+} ions towards the cathode (i.e., the outer electrode (2)), yielding a Fe-enriched layer next to the YSZ container. Note that electrode (2) had been applied by painting with Pt past on the internal surface of the YSZ container. Still, the Fe-rich layer lack metallic luster and its thickness are excessive to assume reduction to metallic Fe. Thus, one may assume enhanced concentration of Fe^{2+} and/or Fe^{3+} ions instead.

Transient electrochemical response

The time dependence of current under constant applied cell voltage may reveal changes related to exhaustion of iron oxide in the aluminosilicate melts, and the corresponding accumulated charge may be a guideline to estimate the Faradaic efficiency, as shown in Fig. 10. Except for current spikes due to periodic switching off of the applied voltage for impedance studies, one may identify a minimal in average current, and this is close to conditions when the accumulated charge should correspond to full reduction of iron, considering predominant Fe^{2+} oxidation state in the melt and $\sim$ 100 % faradaic efficiency. This transition is also revealed by the decrease in the slope of cumulative charge. The latter is more evident for cell b1.5cFe, operated at lower applied voltage (1.5 V), possibly because this cell was less affected by side electrochemical reactions and parasitic effects, such as reduction of silicon dioxide, as shown above. Though a significant fraction of Fe^{3+} would require greater cumulative charge, this may only account for up to 1/3 of the total charge required to reduce Fe^{n+} ions.
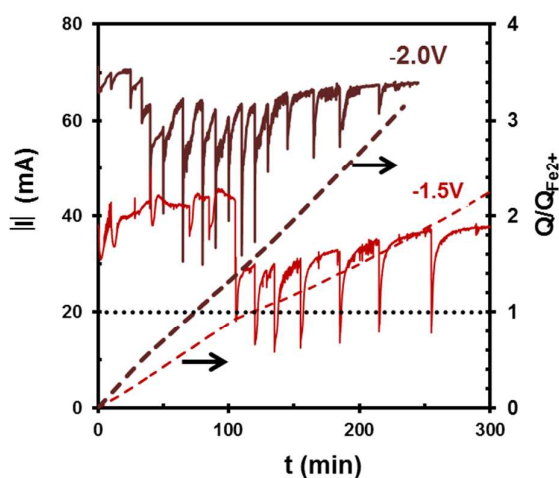

Figure 10 – Time dependence of current (solid lines) under applied voltage of -2V (b2cFe cell) and -1.5 V (b1.5cFe cell). Cumulative charge was computed by integration, and its relative range refers to complete reduction of divalent iron oxide $QrefFe^{2+}$ (dashed lines).

Thus, cumulative charge shows that the final stage is determined by parasitic effects, after depletion of the initial contents of iron oxide in the molten silicate, with corresponding decrease in overall Faradaic efficiency.

Cell b1.5c was also tested with blocking-electron configuration, but in Fe-free MAS electrolyte. Thus, the time dependence of current (Fig. 11) should be ascribed exclusively to parasitic electrochemical reactions. This parasitic current increases gradually, approaching the last stage of cell b1.5cFe with 2 mol% iron oxide This confirms that parasitic contributions predominate as the contents of iron oxide in the molten electrolyte is depleted. Still, the cathode in cell b1.5c retains its morphologic stability. Thus parasitic current should not be exclusively related to disintegration of Pt cathode.
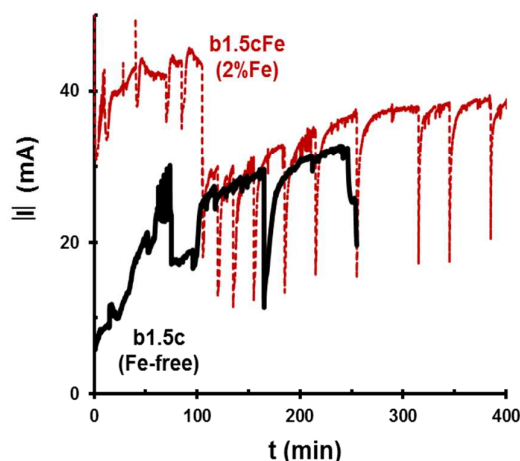

Figure 11 – Comparison of time dependence of current for cells operating with applied cell voltage -1.5V, for the MAS melts with 2 mol% Fe (b1.5cFe cell) and the Fe-free melt (b1.5c cell).

Cell d1.5aFe was operated without electron blocking, i.e., using the central Pt electrode (1) as anode and electrode (2) as cathode (Fig. 12). This cell was also modified to include a stopper at the bottom of the inner Pt electrode to maintain its vertical alignment, thus preventing its drift. Note that long term drift of the central Pt cathode, towards the inner surface of the YSZ container, may cause decrease in the resistance due to changes in effective geometry. This may account, at least partly, to long term increase in current recorded for cells b2cFe, b1.5cFe and b1.5c, whereas cell d1.5aFe shows long term stability.
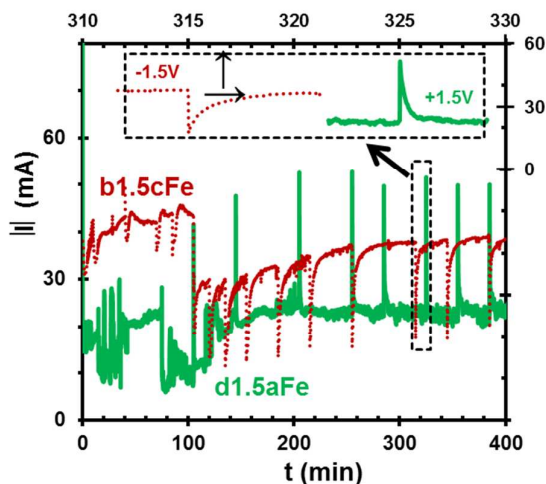
Figure 12 – Comparison of time dependence of current for d1.5aFe and b1.5cFe cells.

Another significant difference between cells d1.5aFe and b1.5cFe is the reversed transient response after temporary interruptions to monitor electrical properties by impedance spectroscopy, i.e., decrease in current on re-establishing anodic polarization of the central Pt electrode, after the initial peak (cell d1.5aFe), and increase in current on re-establishing cathodic polarization, after an initial minimum (cell b1.5cFe). This can be ascribed to redox changes induced by cathodic or anodic polarization and corresponding changes in conductivity, as expected on changing the fugacity of O_2.[37] In addition, the concentration of positively charged carriers may drop close to the positive electrode, as revealed by EDS maps (Fig. 9).

Transient changes in conductivity

Impedance spectra recorded on disconnecting the applied voltage during operation of different cells (Figs. 2 and S2, S3 from ESI) were used to extract corresponding changes in conductivity (Fig. 13). The spectra reveal mainly the intermediate frequency arc, ascribed to an interfacial contribution (Fig. 14), whereas the upper limit of frequency range (10^6 Hz) is insufficient to resolve the contribution at higher frequencies; this was ascribed to the ohmic resistance of the molten MAS (Fig. 13). In addition, the spectra obtained for cell d1.5aFe (Fig. S3, ESI) shows onset of a low frequency contribution, and its nearly linear Z" vs Z' dependence resembles the Warburg impedance of diffusion controlled limitations. However, its slope is significantly lower than expected, and

suggests anomalous diffusion,[55] possibly because the concentration of charged species is time dependent, as emphasized also by the transient response on re-establishing the applied potential (Fig. 12).

This is more likely to occur when the central Pt electrode is under anodic polarization (cell d1.5aFe), thus causing local depletion of positively charged carriers (Fe^{2+}). Indeed, the transient response time shown in Fig. 12 (in the order of 1 min) is several orders of magnitude longer than the reciprocal frequency range of the equipment ($\leq 0.05s$), thus preventing a clear impedance analysis of the diffusion controlled processes. The impedance spectra for cell b1.5cFe (Fig. S2, ESI) are not conclusive about diffusion limitations at lower frequencies.
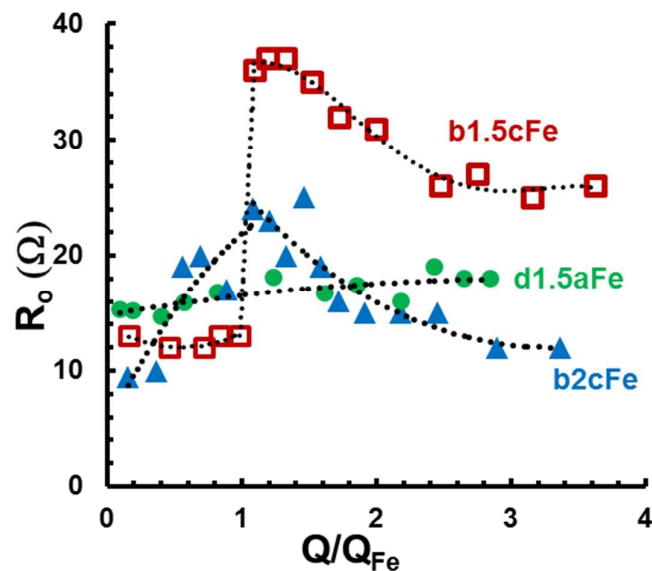

Figure 13 – Dependence of ohmic resistance on relative charging Q/Q_{Fe}, where Q_{Fe} denotes the charge required to reduce the actual content of iron oxide to metallic Fe, assuming that Fe^{2+} prevails.
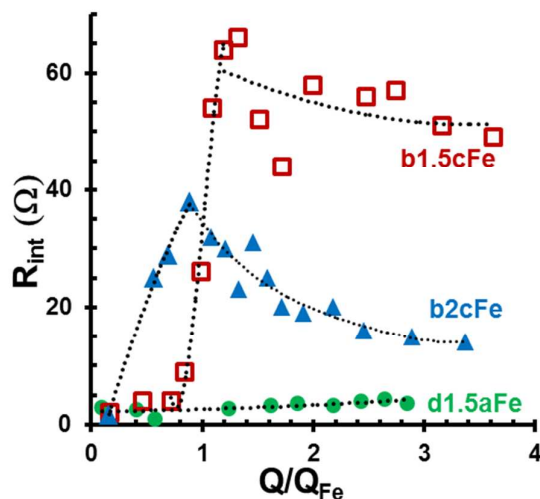
Figure 14 – Dependence of interfacial resistance on relative charging Q/Q_{Fe}, where Q_{Fe} denotes the charge required to reduce the actual content of iron oxide to metallic Fe, assuming that Fe^{2+} prevails.

Fig. 13 confirms sharp increase in ohmic resistance for cells b2cFe and b1.5cFe, on approaching the cumulative charge expected for reduction of Fe^{2+} to metallic Fe, and corresponding depletion of charge carriers. This trend is reverted for greater charging, which is also indicative that parasitic currents increase gradually as the actual concentration of Fe^{n+} vanishes. On the contrary, the direct electrolysis cell d1.5aFe, with central anode, only shows slight increase in ohmic resistance, without any evidence that this will go through a maximum. This confirms that depletion of charge carriers is less effective in this case, consistent with the EDS maps showing accumulation of Fe^{2+} next to the cathode (Fig. 9), and indicating that reduction to metallic Fe is marginal. Thus, Faradaic efficiency is very low in this case.

The dependence of interfacial resistance on relative charging also confirms major differences between direct electron blocking cells (b2cFe and b1.5cFe) and the electrolysis cell d1.5aFe. Depletion of Fe^{2+}, upon reduction to metallic Fe, also causes drastic increase in interfacial resistance and clearly different trends on exceeding the nominal charge required for reduction. On the contrary, the interfacial resistance remains low in the case of cell d1.5aFe, possibly due to a significant contribution of electronic transport, and without significant decay. This behavior also confirms that faradaic efficiency is low in this case.

Changes in interfacial capacitance for cell b1.5cFe (Fig. S4, ESI) also reveal the main

differences between the electrochemical behaviour at relatively low charging, and after exceeding the nominal charging required for reduction of Fe^{2+} to Fe. The initial stages may comprise increase in effective interfacial area by deposition of metallic Fe, the opposite trend at the onset of disintegration of the Pt cathode, and then a major drop in capacitance as the overall behavior becomes controlled by parasitic currents. This is also consistent with evidence that disintegration of the Pt cathode involves alloying with Fe, as shown above.

Concluding remarks on long term parasitic current

Post-morten analysis of cell d1.5aFe does no show evidence of reduction to metallic Fe and in situ monitoring by impedance spectroscopy also failed to show evidence of significant changes upon exceeding the cumulative charge required for complete reduction to metallic Fe.

Thus, the behaviour of this cell should be mainly due to a combination of parasitic effects or electronic leakage, combined with accumulation of carriers next to the outer electrode (cathode) and depletion next to the central electrode (anode), as revealed in Fig. 9. The most likely hypothesis is electron hopping between Fe^{2+} and Fe^{3+}, combined with corresponding charge transfer reactions at cathode ($Fe^{3+}+e' \rightarrow Fe^{2+}$) and at the anode ($Fe^{2+} \rightarrow Fe^{3+}+e'$). Dependence of conductivity on redox conditions or anodic polarization may also cause excessive increase in ohmic losses, near the central electrode (anode), lowering the actual difference between applied voltage (1.5 V) and ohmic losses ($V_{appl} - I R_O$).

Thus, reduction to metallic Fe will be halted if this drops below the required Nernst potential (~ 1.02V). In fact, ohmic resistance extracted from impedance spectra under open circuit conditions (Fig. 13) are clearly underestimated in the case of cell d1.5aFe, due to dependence of resistivity on O_2 fugacity or anodic polarization. The transient response in Fig. 12 suggests that resistance under anodic polarization increases by a factor greater than 2, implying that the ohmic resistance in Fig. S3 (ESI) may increase to values above 30 Ω when current attains a nearly steady value of about 25 mA. This yields ohmic losses exceeding 0.75 V, and V_{appl}-IR_O < 0.75 V, except possibly at short

times or during the transient responses (Fig. 12). In this case, faradaic efficiency should be very low and the long term current may be ascribed to electronic leakage.

The impact of ohmic losses should be much lower for cells b2cFe and b1.5cFe, due to the positive effect of cathodic polarization on conductivity, near the central electrode, as revealed by the transient spikes in Fig. 12. Thus, one still expects conditions required for reduction to metallic Fe ($V_{appl} - IR_O > 1.02$ V), and high faradaic efficiency is expected by hindering electronic leakage via the electron blocking YSZ membranes. Still, this cannot explain the long term current when the cumulative charge exceeds largely the nominal charge required for complete reduction to metallic Fe. A plausible explanation was proposed above, based on reduction of silica to metallic Si, mainly for cell b2cFe, yielding low melting liquid phases in the ternary system Fe-Si-Pt. Disintegration of the Pt cathode may also be taken as a footprint of this parasitic effect. Still, this cannot explain parasitic effects observed also for cells operating in Fe-free molten MAS (cell b1.5c).

Thus, one should also consider other parasitic contributions for the long term current in electron-blocking cells, mainly as the aluminosilicate melt approaches Fe-lean conditions. Plausible additional parasitic effects may be related to contributions of atmospheric gases such as O_2 and humidity, which are known to dissolve in basaltic melts, depending on temperature (T), total pressure (P), water vapour partial pressure (pH_2O) and non-bridging oxygen per unit oxygen (NBO/O):[56]

$$\ln\{wt\% H_2O\} = 0.54 \ln(pH_2O) + 1.24[NBO/O] - 2.95 + 0.02(P/T) \qquad (21)$$

where

$$\ln(\text{NBO/O}) = \frac{2\{X_{K2O} + X_{Na2O} + X_{CaO} + X_{MgO} + X_{FeO} - X_{Al2O3}\}}{\{2X_{SiO2} + 2X_{TiO2} + 3X_{Al2O3} + X_{K2O} + X_{Na2O} + X_{CaO} + X_{MgO} + X_{FeO}\}} \qquad (22)$$

If one assumes this dependence for the actual MAS compositions and for typical conditions T = 1728 K, P = 1 atm and $pH_2O \sim 0.03$ atm one predicts ~ 0.0083 wt% H_2O. This is, indeed, a very low concentration. Still, the corresponding OH groups represent a significant fraction of non-bridging oxygen (0.086). Dissolved water is also known for its impact on the electrical conductivity of aluminosilicate melts[25] and on diffusivity of oxygen, as emphasized by major differences in O^{18} diffusivity for hydrous and anhydrous conditions.[23]

Water dissolution in silicate melts may occur in a variety of forms, including molecular H_2O, hydroxyl groups and even molecular H_2 under reducing conditions.[23,24,57] Still, hydroxyl groups ($\equiv Si - OH$) are likely to prevail for relatively low water contents and for high alumina contents,[57] thus contributing to break bonding oxygen ions:

$$\equiv Si - O - Si \equiv + H_2O \rightarrow 2 \equiv Si - OH \qquad (23)$$
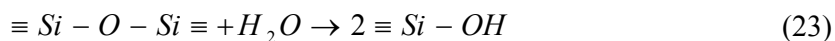
There is also evidence that H_2 can evolve from aluminosilicate melts, and the fugacity of H_2 is expected to increase under reducing condition,[57,59] mainly in the presence of Pt, this may account also for a plausible alternative cathodic reaction:

$$2 \equiv Si - OH + 2e^- \rightarrow H_2(g) + 2 \equiv Si - O^- \qquad (24)$$
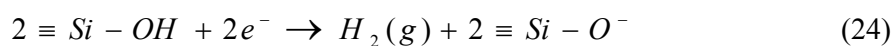
Thus, humidity uptake may sustain alternative cathodic reactions while providing also non-bridging oxygens to sustain oxygen ion transfer at the melt/YSZ interface.

Conclusions

High-temperature iron extraction from the molten magnesium aluminosilicate-based electrolyte was studied in solid electrolyte cells by electrochemical methods, combined with post-mortem SEM/EDS techniques.

The cell comprised an YSZ closed-end tube and three platinum electrodes for conducting pyroelectrolysis experiments. The impedance spectroscopy allowed in-situ monitoring of changes in ohmic resistance and relevant interfacial processes. Various experiments under potentiostatic conditions were performed at 1728 K in electron-blocking cell regime and using direct electrolysis mode. The results of post-mortem microstructural analysis and EDS mapping for the transverse sections of the cell confirmed iron deposition at the cathode, followed by alloying with platinum. The observed trends for changing of the electrolysis current and electrolyte resistance with time suggest high faradaic efficiency under electron-blocking conditions until depletion of the Fe-contents in the aluminosilicate melts.

Still, a conclusive proof of concept for pyroelectrolysis with electron blocking requires alternative electrode materials, to overcome the observed disintegration of the Pt cathode, Pt-Fe alloying, and to sustain high faradaic efficiency as the contents of iron oxide decreases. Efficiency is likely to depend on the actual contents of iron oxide in the aluminosilicate melt, applied voltage and relative cumulative charging. A significant limitation on faradaic efficiency was ascribed to the onset of reduction of silica to metallic Si. Its inclusion in low-melting Fe-Si-Pt liquid phase is also a plausible explanation for disintegration of the Pt cathode. Other plausible parasitic limitations on faradaic efficiency may be related to uptake of atmospheric gases such as humidity or oxygen. These may also sustain alternative cathodic reaction and transfer of oxygen ions across the melt/YSZ interface.

The efficiency of the iron separation from the melt by direct electrolysis process was found very poor, probably due to onset of electronic leakage, and also because the applied voltage is insufficient to account for the combined contributions of ohmic losses and Nernst potential required for reduction to metallic Fe. Since the electrolyte composition, studied in the present work, was limited to one magnesium aluminosilicate-based compound with minimum liquidus temperature, further increase in

the efficiency may be expected from tuning Al to Si ratio to decrease the viscosity of the melt, with corresponding impact on the cations mobility, and to suppress hopping conduction between Fe^{2+}/Fe^{3+} ions, contributing to the electronic leakage.

Acknowledgements

References

1 – C.H.P. Lupis, *Metallurg. Mat. Trans. B*, 1999, **30B**, 841.

2 – M. Barati, *Energy*, 2010, **35**, 3731.

3 – D.R. Sadoway, *J. Mater. Res.*, 1995, **10**, 487.

4 – R.H. Aiken, US Patent, 1906, 816142.

5 – H. Kim, J. Paramore, A. Allanore, D.R. Sadoway, J. Electrochem. Soc., 2011, **158**, E101

6 – D. Wang, A.J. Gmitter, D.R. Sadoway, *J. Electrochem. Soc.*, 2011, **158**, E51.

7 – A. Allanore, L. Yin, D.R. Sadoway, *Nature*, 2013, **497**, 353.

8 – L.A. Haskin, R.O. Colson, D.J. Lindstrom, R.H. Lewis, K.W. Semkow, *NASA Conference Publication*, 1992, *1*, 411.

9 – A. Martin, J.C. Poignet, J. Fouletier, M. Allibert, D. Lambertin, G. Bourgès, *J. Appl. Electrochem.*, 2010, **40**, 533.

10 – U.B. Pal, A.C. Powell, *JOM*, 2007, **59**, 44.

11 – U.B. Pal, D.E. Woolley, G.B. Kenney, *Emerging JOM*, 2001, **53**, 32.

12 – A. Martin, D. Lambertin, J.C. Poignet, M. Allibert, G. Bourges, L. Pescayre, J. Fouletier, *JOM*, 2003, **55**, 52.

13 – A. Krishnan, X.G. Lu, U.B. Pal, *Scand. J. Metallurgy*, 2005, **34**, 293.

14 – H.J. Park, G.M. Choi, *J. Eur. Ceram. Soc.*, 2005, **25**, 2577.

15 – H.W. Koo, H.J. Park, G.M. Choi, H.G. Lee, *ISIJ International*, 2007, **47**, 689.

16 – Y.M. Gao, B. Wang, S.B. Wang, S. Peng, *J. Min. Metall. Sect. B-Metall.*, 2013, **49B**, 49.

17- H. Mao, O. Fabrichnaya, M. Selleby, B. Sundman, *J. Mater. Res.*, 2005, **20**, 975.

18 – A. Lugovskoy, M. Zinigrad, D. Aurbach, Z. Unger, *Electrochim. Acta*, 2009, **54**, 1904.

19 – G. Ottonello, R. Moretti, L. Marini, M.V. Zuccolini, *Chemical Geology*, 2001, **174**, 157.

20 – J.A. Duffy, *Geochimica et Cosmochimica Acta*, 1992, **57**, 3961.

21 – V. Magnien, D.R. Neuville, L. Cormier, J. Roux, J.L. Hazemann, D. de Ligny, S. Pascarelli, I. Vickridge, O. Pinet, P. Richet, *Geochimica et Cosmochimica Acta*, 2008, **72**, 2157.

22 – F. Gaillard, M. Pichavant, B. Scaillet, *Geochimica et Cosmochimica Acta*, 2003, **67**, 4389.

23 – H. Behrens, Y. Zhang, M. Leschik, M. Wiedenbeck, G. Heide, G.H. Frischat, *Earth and Planetary Science Letters*, 2007, **254**, 69.

24 – H. Behrens,Y. Zhang, *Contrib. Mineral. Petrol.*, 2009, **157**, 765.

25 – A. Pommier, F. Gaillard, M. Pichavant, B. Scaillet, *J. Geophys. Res.*, 2008, **113**, B05205.

26 – R. Morelli, *Annals of Geophysics*, 2005, **48**, 583.

27 – V.C. Kress. I.S.E. Carmichael, *Amer. Mineralogist*, 1988, **73**, 1267.

28 – G. S. Nikolaev, A. A. Borisov, A. A. Ariskin, *Geochemistry International*, 1996, **34**, 641.

29 – A. Berry, H.S.C. ONeill, K.D. Jayasuriya, S.J. Campbell, G.J. Foran, *Amer. Mineralogist*, 2003, **88**, 967.

30 – N.M. Ferreira, A.V. Kovalevsky, J.C. Waerenborgh, M. Quevedo-Reyes, A.A. Timopheev, F.M. Costa, J.R. Frade, J. Alloys Comp., 2014, **611**, 57.

31 – H.S.C. O´Neill, S.M. Eggins, *Chemical Geology*, 2002, **186**, 151.

32 – B.O. Mysen, D. Virgo, C.M. Scarfe, D.J. Cronin, *Amer. Mineralogist*, 1985, **70**, 487.

33 – C. Weigel, L.Cormier, G. Calas, L. Galoisy, D.T. Bowron, *J. Non Cryst. Solids*, 2008, **354**, 52.

34 – L. Murawski, *J. Mat. Sci.*, 1982, **17**, 2155.

35 – N.S. Choudhury, J.W. Patterson, *J. Electrochem. Soc.*, 1971, **118**, 1398.

36 – T.H. Etsell, S.N. Flengas, *J. Electrochem. Soc.*, 1972, **119**, 1.

37 – A. Pommier, F. Gaillard, M. Pichavant, *Geochimica et Cosmochimica Acta*, 2010, **74**, 1653.

38 – W.M. White, Geochemistry, Wiley-Blackwell, 2013.

39 – R.L.A. Everman, R.F. Cooper, *J. Amer. Ceram. Soc.*, 2003, **86**, 487.

40 – R.F. Cooper, R.L.A. Everman, J.W. Hustoft, S.H.D. Shim, *Amer. Miner.*, 2010, **95**, 810.

41 – N.R. Bennett, J.M. Brenan, K.T. Koga, *Geochimica et Cosmochimica Acta*, 2014, **133**, 422.

42 – C.E. Ford, *Miner. Magaz.*, 1978, **42**, 271.

43 – T.L. Grove, *Contrib. Mineral. Petrology*, 1981, **78**, 298.

44 – G. Parry, O. Ostrovski, *Met. Mat. Trans.B*, 2008, **39B**, 681.

45 – A. Ricolleau, Y. Fei, A. Corgne, J. Siebert, J. Badro, *Earth and Planetary Sci. Lett.*, 2011, **310**, 409.

46 – S.K. Cho, F. Ren, F. Fan, A.J. Bard, *Electrochimica Acta*, 2012, **65**, 57.

47 – L.L. Xu, J. Wang, H.S. Liu, Z.P. Jin, *Calphad*, 2008, **32**, 101.

48 – W.C. Yang, H. Ade, R.J. Nemanich, *Phys. Rev.*, 2004, **B69**, 045421.

49 – H. Jeong, T.E. Park, H.K. Seong, M. Kim, U. Kim, H.J. Choi, *Chem. Phys,. Lett.*, 2009, **467**, 331.

50 – J. Lacaze, B. Sundman, *Metall. Trans.A*, 1991, **22A**, 2211.

51 – Z.K. Liu, Y.A. Chang, Metall. *Mat. Trans.*, 1999, **30A**, 1081.

52 – M. Nagamori, I. Malinski, A. Claveau, *Met. Trans. B*, 1986, **17B**, 503.

53 – O. Braaten, A. Kjekshus, H. Kvande, *JOM*, 2000, **52**, 47.

54 – C. Smit, R.A.C.M.M. van Swaaij, H. Donker, A.M.H.N. Petit, W.M.M. Kessels, M.C.M. van de Sanden, *J. Appl. Phys.*, 2003, **94**, 3582.

55 – J. Bisquet, A. Compte, *J. Electroanal. Chem.*, 2001, **499**, 112.

56 – G. Iacono-Marziano, Y. Morizet, E. Le Trong, F. Gaillard, *Geochimica et Cosmochimica Acta*, 2012, **97**, 1.

57 – A. Kadik, F. Pineau, Y. Litvin, N. Jendrzejewski, I. Martinez, M. Javoy, *J. Petrology*, 2004, **45**, 1297.

58 – W.J. Malfait, *Amer. Miner.*, 2014, **99**, 1648.

59 – A.A. Kadik, N.A. Kurovskaya, Yu.A. Ignat'ev, E.B. Kryukova, V.V. Koltashev, N.N. Kononkova , *Geochem. Int.*, 2013, **51**, 1019.